Rotationally inelastic scattering of O3–Ar: state-to-state rates with the multiconfigurational time dependent Hartree method

Sangeeta Sur, Steve A Ndengué, Ernesto Quintas-Sánchez, Cheikh Bop, François Lique, Richard Dawes

Rotationally inelastic scattering of O_3–Ar: State-to-state rates with the MultiConfigurational Time Dependent Hartree method

Sangeeta Sur,[†] Steve A. Ndengué,[†,‡] Ernesto Quintas-Sánchez,[†] Cheikh Bop,[¶] François Lique,[¶] and Richard Dawes[*,†]

[†]*Department of Chemistry, Missouri University of Science & Technology, Rolla, MO 65401, USA*

[‡]*ICTP-East African Institute for Fundamental Research, University of Rwanda, Kigali, Rwanda*

[¶]*LOMC - UMR 6294, CNRS-Université du Havre, 25 rue Philippe Lebon, BP 1123, F-76063 Le Havre, France.*

E-mail: dawesr@mst.edu

Abstract

The Chapman cycle, proposed in 1930, describes the various steps in the ongoing formation and destruction of stratospheric ozone. A key step in the formation process is the stabilization of metastable ozone molecules through collisions with a third body, usually an inert collider such as N_2. The "ozone isotopic anomaly" refers to the observation of larger-than-expected atmospheric concentrations for certain ozone isotopologues. Previous studies point to the formation steps as the origin of this effect. A possibly key aspect of the ozone formation dynamics is that of the relative

efficiencies of the collisional cooling of different isotopologues. Although the substitution of low-abundance ^{18}O for ^{16}O in O_3 molecules corresponds to a relatively small net change in mass, related to this are some subtleties due to symmetry-breaking and a resulting more than doubling of the density of allowed states governed by nuclear-spin statistics for bosons. Recently, a highly accurate 3D potential energy surface (PES) describing O_3–Ar interactions has been constructed and used to benchmark the low-lying rovibational states of the complex. Here, using this new PES, we have studied the collisional energy-transfer dynamics using the MultiConfiguration Time Dependent Hartree method. A study of the rotationally inelastic scattering was performed for the parent $^{16}O^{16}O^{16}O$–Ar system and compared with that of the $^{16}O^{16}O^{18}O$–Ar isotopologue. The state-to-state cross-sections and rates from the $0_{0,0}$ initial state to low lying excited states are reported. Analysis of these results yields insight into the interplay between small changes in the rotational constants of O_3 and the reduced mass of the O_3–Ar collision system, combined with that of the symmetry-breaking and introduction of a new denser manifold of allowed states.

Introduction

Mass-independent fractionation of ozone—leading to anomalous column densities of the heavier isotopologues—is a well-known occurrence consistently observed in the stratosphere as well as in laboratory experiments.[1,2] Although this phenomenon has been the subject of numerous theoretical[3,4] and experimental[5–7] studies since its discovery in the 1980s, and several relevant factors have been identified,[8–15] a quantitatively-predictive model for the complete set of isotopic species has been elusive.

Oxygen has three stable isotopes: ^{16}O, ^{17}O and ^{18}O. In Earth's atmosphere, ^{16}O is dominant with an abundance of nearly 99.8%, while there is roughly five times more ^{18}O than the other trace ^{17}O isotope. Thus most ozone is found as the $^{16}O^{16}O^{16}O$ parent species, with trace amounts of the other isotopologues. Following a common convention, the $^{16}O^{16}O^{16}O$

isotopologue will be hereafter referred to as 666, while $^{16}O^{18}O^{16}O$ will be referred to as 686, and $^{16}O^{16}O^{18}O$ as 668, etc. In the early 1980s, enrichments of heavy O_3 molecules were observed by Mauersberger[16,17] in the stratosphere and were reproduced by Thiemens[18] in the laboratory. These enrichments, defying mass-dependent expectations, are almost equal in ^{17}O and ^{18}O, and thus came to be known as the "mass-independent fractionation," or the "isotopic anomaly effect" of ozone. To gain insight into this phenomenon, numerous experiments were carried out, and the isotope selectivity was ultimately traced back to the recombination step[19–23] in the formation process of ozone, described by the Chapman cycle.[24] The recombination process of O_3 is a three-step process as shown below:

$$O_2 + O + M \rightarrow O_3^* + M \tag{1}$$

$$^yO^zO + {}^xO \rightarrow O_3^* \rightarrow {}^xO^zO + {}^yO \quad \text{or} \quad {}^yO^xO + {}^zO \tag{2}$$

$$O_3^* + M \rightarrow O_3 + M^* \tag{3}$$

The formation step (1) of the process, involves an O-atom combining with an O_2 molecule to form a rovibrationally metastable O_3^* molecule. To complete the formation, this is followed by the stabilization step (3), which involves the sufficiently long-lived metastable resonance state of O_3^* colliding with a third body, M, to form stable O_3. The third body, M, is any encountered quencher undergoing inelastic collision such as N_2, O_2 or Ar, the identity of which does not significantly affect the fractionation.[25,26] In addition to the posssibility of stabilization via a cooling collision, there is a competing exchange process, step (2), where the superscripts label the three possible isotopes.

Numerous theoretical studies have investigated both the exchange and competing formation processes. These include statistical approaches,[12–14] and treatments based on the differing symmetries and densities of allowed quantum states governed by nuclear-spin statistics for isotopologues such as 666 and 668. A number of potentially relevant factors or explanations have been put forward. Substitution reactions replacing ^{16}O with heavier isotopes

are very slightly exothermic due to the changes in zero-point energy. The dynamics of the metastable resonances (O_3^*), found to affect the rates of isotopic exchange reactions,[3] also then affect the competing rates of formation. Many of these factors can be shown to play a role, but still—as mentioned above—a quantitatively predictive model for all observed abundancies is still lacking. Nonadiabatic effects, with spin-orbit and derivative couplings between low-lying singlet, triplet, and quintet electronic states have also been considered; and while not currently held as a leading explanation, have not been fully discounted (mostly due to the complexity and computational cost of such simulations). Indeed, direct simulation of the dynamics, even for the exchange processes, has been hindered by the complexity of ozone's electronic structure. A spurious barrier in the entrance channel for approach of the O-atom to the O_2 molecule is common to many—even very high-level—electronic structure methods, and causes large discrepancies in the rates of exchange computed using these potential energy surfaces (PESs).[27–29] In the presence of a spurious barrier in the PES, a qualitatively incorrect positive temperature-dependence is obtained for the exchange rates, in contrast to the steep negative temperature-dependence observed experimentally. In addition, the spurious barrier traps spurious Van der Waals (vdWs) type states near the dissociation limit. These states are physically unrealistic in character, and thus have hindered insight into the role of high-lying bound and resonance states in the dynamics governing the exchange and formation processes. Since 2011 the barrier has been understood to be spurious,[27] and accurate monotonically-attractive PESs were reported in 2013.[28,30] Using these PESs key aspects of the exchange processes (such as the rates and their temperature dependencies) have been reproduced satisfactorily in several quantum dynamics studies.[3,31–33]

Of course the formation process, involving a third-body collider, is considerably more complex. Nevertheless, a significant number of theoretical studies, especially those by the group of Babikov, have explored the formation steps.[8,12–14,34–38] Babikov has put forth a hierarchy of theoretical models analyzing the underlying systems of kinetics at different levels of sophistication. So far, in all of these models a remaining assumption/approximation has

been that the rates of collisional cooling for different O_3 isotopologues are the same.[11] In quantum inelastic scattering studies of small systems, relevant for instance to the interstellar medium,[39–41] this has frequently been found to not be the case. It is noted that there is a more than doubling of the density of allowed rovibrational states when the symmetry of O_3 is broken moving from 666 to 668, owing to a small degree to the slight mass change, and mostly due to nuclear-spin statistics.[42] Significant changes in scattering cross-sections have been observed upon isotopic substitution, in some cases where the center-of-mass shift is small, in the absence of symmetry-lowering and even without significantly different state densities.[40] This could affect the inelastic collisional cross-sections and corresponding rate coefficients, and thus impact modeling of the ozone isotopic anomaly.

A major difficulty for studying collisional energy transfer in ozone is again the lack of an accurate available PES. Direct simulation of step (3) with resonances above the dissociation limit as the initial states, would require a fully flexible 6D PES, and the quantum scattering calculations would also be very challenging. Recently, the electronic structure for the flexible O_3–Ar system (M = Ar for simplicity) has been benchmarked,[43] and a protocol suitable to construct the full 6D PES was identified. It was also determined that some of the relevant issues could be explored within the rigid rotor approximation, requiring only a 3D PES. These include symmetry-breaking and the corresponding change in allowed states; the corresponding shift in center-of-mass and effective skewing of the PES; changes to the rotational constants of O_3; and a change in the reduced mass of the collision system. The rigid rotor approximation simplifies both the PES construction and subsequent scattering dynamics. Thus a new 3D PES was constructed for the O_3–Ar system employing the derived electronic structure protocol. Rovibrational vdWs states were computed and reported using the new PES. Comparisons with microwave experiments confirm its high-accuracy.[44]

In this study, the inelastic collision processes of O_3 with Ar have been studied using a time-dependent quantum mechanical approach. A major concern with fully quantum approaches is the poor (exponential) scaling of the computational costs with system-size (dimensionality)

and complexity (density of states), which is also known as the "curse of dimensionality." Here, the MultiConfigurational Time Dependent Hartree (MCTDH) method is used to study the collisional dynamics of this system. This method has been previously used to study inelastic scattering[45–48] in medium-sized asymmetric top molecules and is sufficiently efficient to enable the currently reported study.

Inelastic state-to-state cross-sections and rates for the 666 and 668 O_3–Ar isotopologues are reported for collisions from the ground ($0_{0,0}$) initial state, to a number of low-lying excited product states. The results for the two systems are compared and trends and propensities are identified, some of which are in conflict with the often employed exponential-gap-based model.[49–51] Exponential-gap models, recognizing the importance of state density, estimate inelastic scattering transition rates solely based on the energy-differences between states (the dependence is assumed to be exponential in the gap-size, hence the name). Although often found to be too simplistic, these methods, needing only the energy levels, have the advantage of not requiring any computationally expensive scattering calculations. (Note that a simple exponential-gap model, implemented for this system without any regard or refinements for propensities, would strongly favor collisional cooling of 668 relative to 666...). Finally, the likely relevance of isotopologue-specific collisional cooling rates to the observed stratospheric fractionation is discussed.

Methodology

Reference frame, coordinates, and PES

The coordinates used to define the 3D PES are R, θ and ϕ; where R represents the distance between the center-of-mass of the ozone molecule and the argon atom, while θ and ϕ represent the spherical angles as shown in Figure 1. The ozone molecule is fixed in the xz plane, with the origin of the frame of reference at its center-of-mass.

In a previous study,[43] we benchmarked the electronic structure for the O_3–Ar sys-

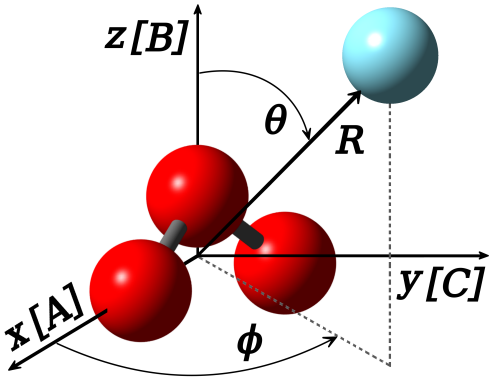

Figure 1: 3D body-fixed (principal-axis) Cartesian coordinate system used to describe the O_3–Ar interaction. Also labeled are the corresponding A, B and C inertial axes.

tem within the rigid rotor approximation—keeping the structural parameters of the ozone molecule fixed at their equilibrium position:[28] $r_1 = r_2 = 1.2717$ Å and $\alpha = 116.84°$. A well-depth for the complex of 229.4 cm^{-1} was determined at the CCSD(T)-F12b/CBS level, and a 3D PES was constructed at this level of electronic structure theory. In anticipation of a future flexible 6D PES, a multireference-based protocol was also established employing MRCI calculations for which a procedure of scaling the correlation energy was developed and proved to be successful in closely matching the coupled-cluster benchmark. The 3D PES was constructed using an automated interpolating moving least squares methodology, which has been recently released as a software package under the name AUTOSURF.[52] Using a total of 2712 *ab initio* points, coverage is obtained in the broad coordinate range of 2 Å $< R <$ 25 Å, $0 < \theta < \pi$, and $0 < \phi < 2\pi$; with a global root mean square error (RMSE) lower than 1 cm^{-1}. Rovibrational calculations were performed using the constructed PES and close agreement with microwave experiments on the O_3–Ar complex was obtained, which constitutes an important validation of the accuracy of the PES and hence the level of theory in the underlying electronic structure calculations. In order to use the PES to study interactions of various isotopologues of ozone with Ar, the shift in center-of-mass of the ozone molecule upon isotopic substitution and the associated transformation of the coordinates was determined. This permits use of the PES to describe any other isotopologue of ozone complexed with Ar without performing any additional electronic structure calculations.

MCTDH Calculations

The MCTDH method[53,54] is a time-dependent approach to solve the Schrödinger equation. The method may be considered as a time-dependent version of the MultiConfigurational Self-Consistent Field (MCSCF) method,[55,56] applied in this case to the nuclei. The complete active space (CAS) of MCTDH is composed of time-dependent one- or multi-dimensional functions (forming an orthonormal basis set) written as a sum-of-products (SOP) of single-particle functions (SPFs). The *ansatz* of the MCTDH wave function expressed as a SOP of these SPFs can be represented as

$$\Psi(Q_1,\cdots,Q_f,t)=\sum_{j_1=1}^{n_1}\cdots\sum_{j_f=1}^{n_f}A_{j_1\cdots j_f}(t)\prod_{\kappa=1}^{f}\phi_{j_\kappa}^{(\kappa)}(Q_\kappa,t)=\sum_{J}A_J\Phi_J\ , \tag{4}$$

where f denotes the number of degrees of freedom of the system, $Q_1,\ldots,Q_f$ denote the nuclear coordinates, $A_J{=}A_{j_1\cdots j_f}$ represent the expansion coefficients, and Φ_J are the products of the SPFs or Hartree products. The optimized SPFs are (time-dependent) linear combinations of time-independent primitive basis functions associated with the different degrees of freedom of the system—represented on a Discrete Variable Representation (DVR) grid. The advantage of this method lies in the smaller number of optimized SPFs used compared to the number of functions composing the primitive basis. This reduces the memory and CPU costs of the quantum dynamics calculations. All the calculations reported here were performed using the freely available Heidelberg MCTDH package.[57]

Inelastic scattering calculations using MCTDH requires certain procedures to be followed: constructing the Hamiltonian for the system, generating the initial wave packet, selecting a suitable complex absorbing potential, etc. The required steps have already been discussed in detail previously,[45–48,58–60] and in this article only the basics of the procedure and specific parameters will be described.

Setting up the Hamiltonian

The Hamiltonian for the O_3–Ar system is represented in Jacobi coordinates (*cf.* Figure 1) as the sum of the Kinetic Energy Operator (KEO) and the potential energy operator. Taking the same KEO-representation used in our previous studies,[43] the Hamiltonian of the system in the Body-Fixed (BF) frame, $\hat{H}$, is written as:

$$\hat{H} = -\frac{1}{2\mu_R}\frac{\partial^2}{\partial R^2} + \frac{\hat{\vec{L}}_R^{\dagger}.\hat{\vec{L}}_R}{2\mu_R R^2} + \hat{T}_{O_3} + \hat{V}_{O_3-Ar} \ , \tag{5}$$

where R represents the distance between the Ar atom and the center-of-mass of the O_3 molecule, and μ_R represents the reduced mass of the system. $\hat{V}_{O_3-Ar}$ denotes the intermolecular PES, while $\hat{T}_{O_3}$ represents the KEO of the ozone molecule and $\hat{\vec{L}}_R$ denotes the orbital angular momentum of the system. The product of the orbital momentum with its transpose conjugate can be expanded as:

$$\hat{\vec{L}}_R^{\dagger}.\hat{\vec{L}}_R = \hat{\vec{J}}_{BF}^2 + \hat{\vec{L}}_{O_3,E_2}^2 - 2\hat{J}_{z^{BF}}\hat{L}_{O_3,z^{BF}} - \hat{J}_{-^{BF}}\hat{L}_{O_3,+^{BF}} - \hat{J}_{+^{BF}}\hat{L}_{O_3,-^{BF}} \ , \tag{6}$$

where E_2 is the frame of reference described by Gatti and Iung.[61] The KEO for the ozone molecule, when expressed in polyspherical coordinates—as it is here—is already in a SOP form; and using the rotational constants for the system (A, B and C) can be expressed as:[60]

$$\hat{T}_{O_3} = \frac{(A+C)}{2}\hat{\vec{L}}_{O_3,BF}^2 + \left[B - \frac{(A+C)}{2}\right]\hat{\vec{L}}_{O_3,z^{BF}}^2 + \frac{(A-C)}{4}\left[\hat{\vec{L}}_{O_3,+^{BF}}^2 + \hat{\vec{L}}_{O_3,-^{BF}}^2\right]. \tag{7}$$

As in our previous studies, the rotational constants used for O_3 in the 666 O_3–Ar system are:[62] $A = 3.55366659$ cm^{-1}, $B = 0.44528320$ cm^{-1} and $C = 0.39475182$ cm^{-1}, while the system reduced mass used is 21.80383583 amu. For the 668 O_3–Ar system, the rotational constants used for O_3 are:[62] $A = 3.48818517$ cm^{-1}, $B = 0.42000833$ cm^{-1}, and $C = 0.37400895$ cm^{-1}, while the system reduced mass is 22.20843419 amu.

The fitted PES mentioned before is not in a SOP form and therefore needed to be

Table 1: Parameters of the primitive basis for the inelastic scattering calculations of O_3–Ar. FFT stands for Fast Fourier Transform, Wigner for Wigner-DVR, and Exp. for Exponential-DVR. K is the momentum representation of the first Euler angle. The distance is in bohr and the angles are in radian.

	R	β_{O_3}	γ_{O_3}	α_{O_3}
Primitive basis	FFT	Wigner	Exp.	K
Number of points	768	41	41	21
Range	3.0−45.0	0−π	0−2π	-10,10
Size of SPF basis	40		40	

re-expressed to be used straightforwardly with MCTDH. Using the `potfit` algorithm[63,64] implemented in the MCTDH package, the PES constructed with AUTOSURF was refitted in the SOP form suitable for the inelastic scattering studies. A set of Euler angles (α_{O_3}, β_{O_3} and γ_{O_3}) is defined in the same frame of reference, with the spherical angle θ corresponding to β_{O_3} and ϕ corresponding to γ_{O_3}. The coordinate-transformed PES corresponding to each isotopologue was separately expanded in SOP form for convenience. The `potfit` algorithm is accurate and efficient for low-dimensional systems, and here the relative RMSE of the two SOP expansions are each about 0.15 cm^{-1}. As shown in Table 1, the parameters for the calculations were selected as follows: for the radial coordinate, 768 sine DVR points were placed in the range of $R = [3, 45]$ bohr, while for the angle β_{O_3} 41 Wigner DVR functions[65,66] were used in the $[0, \pi]$ range; 41 exponential DVR points were used in the $[0, 2\pi]$ range for γ_{O_3}. This basis describes rotational states up to $j = 40$ and thus includes many closed channels above the processes considered here. The angular part consists of β_{O_3}, γ_{O_3}, and α_{O_3} (where α_{O_3} is the momentum representation for a particular state and K goes from $-j$ to $+j$, *i.e.*, for $j = 0$ calculations K is 0, while for $j = 1$ calculations, K is -1, 0, 1). For the calculations of higher j ($j > 10$), K is limited to the range of $K = [-10, 10]$, as shown in Table 1.

Generating the initial wave packet

The wave packet defining the initial state of the collision system is constructed as a product of a Gaussian function along coordinate R, and the wave function for the desired initial rotational state of the ozone molecule. Since the wave packet propagates toward the molecule along R, it was constructed at large initial separation, outside the interaction region. The Gaussian energy distribution depends on two parameters. The first is the width of the Gaussian (denoted by σ) and the second is the momentum of the wave packet. An initial impulsion towards the interaction region is required for the initial wave packet to propagate. This is defined by the specified momentum, p. The optimal energy distribution of the Gaussian function, as well as its initial momentum necessary to sample the range of collision energy of interest, is obtained using the `pledstr` program in the MCTDH package. The parameters σ, and p obtained for O_3–Ar are 0.16 a.u and -13 a.u respectively. The negative sign for momentum indicates that the wave packet is moving towards the region of interaction from the long-range, starting at 30 bohr in this case. To construct the initial rotational state for the ozone molecule, a different Hamiltonian is setup, describing the non-interacting molecule, which is expressed as

$$\hat{H}_{init} = -\frac{1}{2\mu_R}\frac{\partial^2}{\partial R^2} + \hat{T}_{O_3} + \hat{V}_{init}(R) \ , \tag{8}$$

where $\hat{V}_{init}(R)$ represents the potential energy. The eigenvalues are then obtained by the diagonalization of $\hat{H}_{init}$. This Hamiltonian is also used to obtain all the product rotational states after the inelastic scattering.

Ozone is an asymmetric top in its electronic ground state. The rotational energy levels for the molecule are described by a set of three quantum numbers (j, K_a and K_c) and will be referred to using the simplified notation: $j_{Ka,Kc}$. ^{16}O and ^{18}O are both spin-zero bosons, and thus the total wave function for any allowed state must be symmetric upon exchange of any two identical O-atoms. The allowed rotational states for the 666 isotopologue in its

Table 2: C_{2v} molecular symmetry group table for the rotational wave function (o = odd, e = even).

C_{2v}	E	C_2	σ_{xz}	σ_{xy}	$\mid K_a K_c >$
A_1	1	1	1	1	e e
A_2	1	1	-1	-1	o o
B_1	1	-1	1	-1	o e
B_2	1	-1	-1	2	e o

Table 3: C_S molecular symmetry group table for the rotational wave function (o = odd, e = even).

C_S	E	C_2	$\mid K_a >$	$\mid K_c >$
$A^{'}$	1	1	e e	o e
$A^{''}$	1	-1	o o	e o

ground vibrational state follow the symmetry of the C_{2v} point group given in Table 2[67] and are restricted to K_a, K_c being either both *even* or both *odd* (see Table 4). (Note that the allowed rotational states change for odd quanta of excitation in the asymmetric vibrational stretching mode ν_3). The 668 isotopologue has the reduced C_S point group symmetry for which all rotational states are allowed (see Table 3). All states have spin function weights of $(2I+1)(I+1) = 1$. The block improved relaxation method,[68–70] which is a time-independent MCSCF-approach to solve the Schrödinger equation, was used to compute the eigenstates of the system. The obtained low-lying rotational energy levels for the 666 and 668 O_3–Ar systems are shown in Table 4.

Parameterization of the complex absorbing potential

To avoid nonphysical reflections at the grid boundaries as the wave packet approaches the edges of the grid, a complex absorbing potential (CAP), which is an imaginary negative potential, is used to absorb the wave packet. A suitably optimized CAP should smoothly absorb the wave packet without producing nonphysical reflections. The CAP can be expressed as $-iW$, where W can be expanded as:

$$W(\chi) = \eta|\chi - \chi_c|^b \Theta(\chi - \chi_c) \ , \tag{9}$$

Table 4: Rotational energy levels (in cm^{-1}) for 666 and 668 O_3–Ar systems.

j_{K_a,K_c}	666	668
$0_{0,0}$	0.00000	0.00000
$1_{0,1}$		0.79402
$1_{1,1}$	3.94842	3.86219
$1_{1,0}$		3.90819
$2_{0,2}$	2.51951	2.38154
$2_{1,2}$		5.40423
$2_{1,1}$	5.72955	5.54223
$2_{2,1}$		14.74676
$2_{2,0}$	15.05531	14.74727
$3_{0,3}$		4.76154
$3_{1,3}$	8.02189	7.71696
$3_{1,2}$		7.99296
$3_{2,2}$	17.57481	17.12881
$3_{2,1}$		17.13138
$3_{3,1}$	33.24343	32.58501
$3_{3,0}$		32.58501
$4_{0,4}$	8.39126	7.93248
$4_{1,4}$		10.80002
$4_{1,3}$	11.78454	11.25999
$5_{0,5}$		11.89232
$5_{1,5}$	15.35141	14.65290
$5_{1,4}$		15.34279

where Θ is the Heaviside step function (χ_c being the starting point), η is the strength of the CAP and b is the order. To optimize the CAP parameters in the energy range of interest for the scattering, the `plcap` program of the MCTDH package is used. The optimized CAP parameters for the 666 and 668 O_3–Ar systems are given in Table 5.

Wave packet propagation

The next step in the calculation is the wave packet propagation. Calculations were setup for total angular momentum (J_{tot}) ranging from 0 to 200. Initial tests were performed with 666 O_3–Ar to confirm the convergence of the CAP as well as the SPF bases. After having confirmed all parameters, propagation calculations were setup and performed for both 666 and 668 O_3–Ar using the same set of parameters, except for small changes in the reduced

Table 5: Parameters of the CAP selected for the inelastic scattering calculations of the 666 and 668 O_3–Ar systems.

	χ_c (bohr)	η (a.u.)	b
666	32.0	1.06551×10^{-8}	4
668	32.0	1.06635×10^{-8}	4

mass, rotational constants, and CAP coefficient η. The primitive and SPF bases selected for the scattering calculations are given in Table 1. This basis is generously complete for the energy range selected for the scattering studies, up to 700 cm^{-1} (staying below the bend vibrational mode of the molecule). The temperature at 30 km elevation in Earth's stratosphere is around 225 K, for which kT corresponds to about 160 cm^{-1}. Adequacy of the basis was confirmed through convergence tests for the SPF basis for $J_{tot} = 0$ while comparing the flux with the energy distribution for a wide range of energy, as depicted in Figure 2. The best chosen SPF should be the one which has flux closest to the Gaussian energy distribution for the system. The energy range used in this study is $[0.001, 0.087]$ eV. Correct performance of the CAP was confirmed by analyzing the time of completion of the propagation. For smaller J_{tot}, the wave packet took longer to be absorbed by the CAP compared to the same fraction of the wave packet being absorbed for larger J_{tot}. Convergence was confirmed for the SPF basis. For the basis to be deemed satisfactory, the population of the least populated natural orbital was monitored. For values of J_{tot} less than 10, the smallest population was consistently below 10^{-4}, while for larger values of J_{tot}, it remained below 10^{-5}. Another test for convergence of the SPF basis was performed by further increasing the SPF basis for the calculation of a J_{tot} in the lower energy region and checking the convergence of the probabilities of the transitions. The populations of the calculations for various SPFs as a function of time for $J_{tot} = 25$ for the two systems are provided in the Supporting Information (SI).

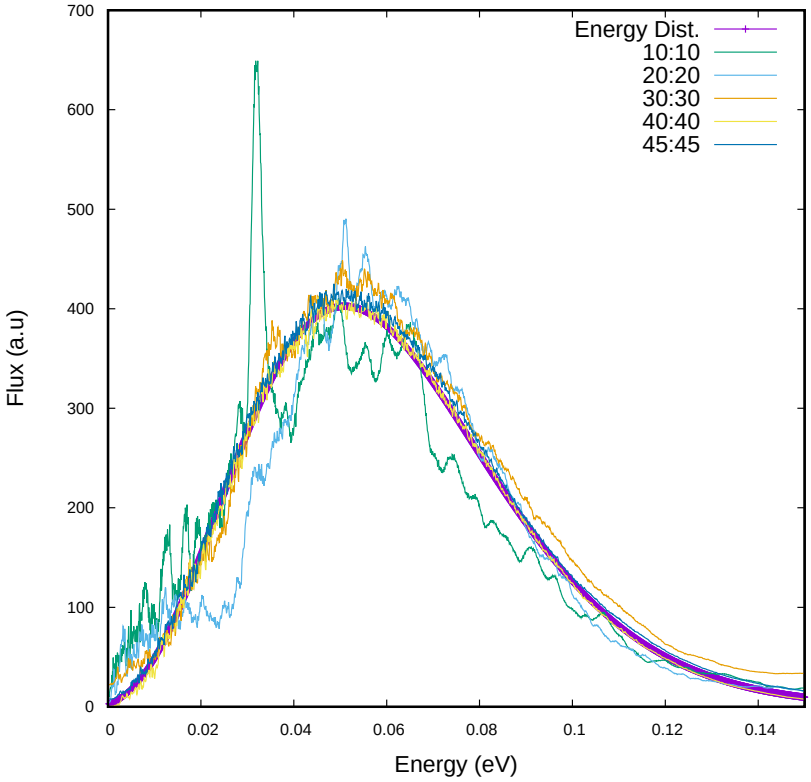

Figure 2: For $J_{tot} = 0$, flux as a function of energy for various sizes of the SPF basis (R:β_{O_3},γ_{O_3},α_{O_3}), radial and angular respectively. "Energy Dist." denotes the energy distribution for the system.

Results and Discussion

Transition Probabilities

The energy range used for the wave packet propagation calculations was $[0.001, 0.087]$ eV, staying just below the fundamental vibrational frequencies for 666 of 1135 cm^{-1} (a_1), 716 cm^{-1} (a_1) and 1089 cm^{-1} (b_2).[71] In fact, the focus here is on the lowest-lying rotational states and the vibrational product channels are considered closed. At this time, with a rigorous fully quantum treatment, it is prohibitively expensive to perform an extensive study including a wide range of initial and product states. However, the qualitative aspects of symmetry breaking due to isotopic substitution and the related changes in state densities hold throughout the bound states. Moreover, the rates of collisional excitation and de-excitation are connected through the principle of detailed balance. The range of total angular momentum considered was $J_{tot} = 0$–200. The convergence of the cross sections with respect to J_{tot} was confirmed and some examples are plotted in SI. As was done in previous studies, it was found that results for many values of J_{tot} could be reliably obtained by interpolation. The smallest values of J_{tot} required more SPFs and longer propagation times, and having cross-sections with more complicated structure, were therefore sampled more densely, while the largest values of J_{tot} require fewer SPFs, complete more quickly, and can be more sparsely sampled. Propagations were performed for J_{tot} =[0–5, 10, 15, 20, 25, 30, 35, 40, 45, 50, 60, 70, 80, 90, 100, 120, 140, 160, 180, 200]. Following the propagations, analysis was performed to obtain the state-to-state probabilities using the Tannor and Weeks[72] method (deemed to be more accurate for the low energies in this application than the alternative flux-based approach). Results for intermediate values of J_{tot} were estimated by interpolation. The interpolations were done very carefully and compared with the computed probabilities (provided in the SI). It is worth mentioning a few differences in how scattering calculations are performed and results obtained using MCTDH as compared to the perhaps more familiar time-independent close-coupling (CC) method. In contrast to CC where one specifies a single precise collision

energy and a generous basis corresponding to open and closed channels (obtaining results for all of them), with MCTDH, the wavepacket covers a broad energy distribution and results are obtained for a range of energies simultaneously. Regarding the basis, as specified in Table 1 we used a very large basis (up to $j = 40$) thus faithfully converging the dynamics, but only performed the final processing for a limited number of product states. Thus, although the number of product states is limited, the results are well converged.

Cross-Sections and Rate Coefficients

Given the probabilities, the inelastic cross-sections for the two isotopologues were calculated from the weighted sum of the probabilities using the relation:

$$\sigma^{jlk}_{j_0l_0k_0}(E) = \frac{\pi\hbar^2}{2\mu_R\big(2j_0+1\big)E_{coll}} \sum_{J_{tot}=0}^{\infty} \big(2J_{tot}+1\big) \sum_{k} \sum_{k_0} P^{J_{tot}}_{jlk\leftarrow j_0l_0k_0}(E) \ , \tag{10}$$

where for the collision system, the orbital angular momentum quantum of O_3 is expressed as j, k is its projection along the Body-Fixed z-axis (intermolecular axis), and l is the projection of j along the monomer z-axis of O_3 and runs from $-j$ to $+j$. Here, we have replaced l by K_aK_c, where K_a and K_c are respectively the projection of the molecular orbital angular momentum along the Body-Fixed (monomer) axis in the prolate and oblate limits. The l values range from $-j$ to $+j$. The derived cross-sections include summation over all the degenerate projections of the angular momentum k.[48] E_{coll} denotes the collision energy, which is the difference between the total energy E and the internal energy of the initial rovibrational state.

The manifold of rotational states for 668 (see Table 4) is slightly more than twice as dense as that of 666. This is due mainly to the introduction of allowed states with $K_aK_c = eo$, or oe (*cf.* Tables 2 and 3), which doubles the number of such states. Furthermore, the slight mass-induced change in the rotational constants slightly contracts the entire ladder of states so that corresponding states for 668 are found at slightly lower energies than for

666. For example, the gap of 3.94842 cm^{-1} between states $0_{0,0}$ and $1_{1,1}$ for 666 is reduced to 3.86219 cm^{-1} for 668. 668 also sees the appearance of the $1_{0,1}$ ($K_aK_c = eo$) state at 0.79402 cm^{-1}, which is not allowed for 666.

The cross-sections obtained for the collision-induced transitions from the ground state to low lying rotational states are represented in Figure 3 for $^{16}O^{16}O^{16}O$ and Figure 4 for $^{16}O^{16}O^{18}O$. All states with $j = 0$–3 as well as some additional states with $j = 4, 5$ (those found below 20.0 cm^{-1}) were included as product-channel states. The left-side panel for each of Figures 3 and 4 plots the cross-sections on a linear-scale against the collision energy on a log-scale. For the lowest states, this shows clearly the energy threshold of each cross-section, matching the rotational energies given in Table 4. The linear-scale for the cross-sections in the left-side panels highlights the dominance of the $0_{0,0} \rightarrow 2_{0,2}$ transition. The right-side panels of Figures 3 and 4 plot the cross-sections on a log-scale against the collision energy on a linear-scale. This obscures the threshold origins, but better illustrates the relative magnitudes of the less dominant transitions. It is clear from these figures that there is a strong propensity towards $\Delta j = 2$ transitions, especially those to states with pure C-axis projections (j_{K_a,K_c}, with $K_a = 0$ and $K_c = j$), *e.g.* $2_{0,2}$ and $4_{0,4}$. The classical visualization of this involves a cartwheeling motion of the O_3 molecule.

Figure 5 compares the cross-sections for transitions to j_{0,K_c} ($K_c = j$) states for both 666 and 668. 668 has the allowed $1_{0,1}$, $3_{0,3}$, and $5_{0,5}$ states in addition to the $2_{0,2}$ and 4_{04} states found in 666. The asymmetry in the PES introduced by the shifted center-of-mass in 668 governs the *odd* Δj transitions to those states. This comes at the expense of the evenness of the PES which governs the *even* Δj transitions to these states in both systems. The shift in center-of-mass is slight and so—as seen in the figure—for 668 the *even* Δj transitions, though slightly reduced compared with 666, are still dominant. Within the sets of *even* or *odd* Δj transitions, as expected, cross-sections decrease for larger changes in j.

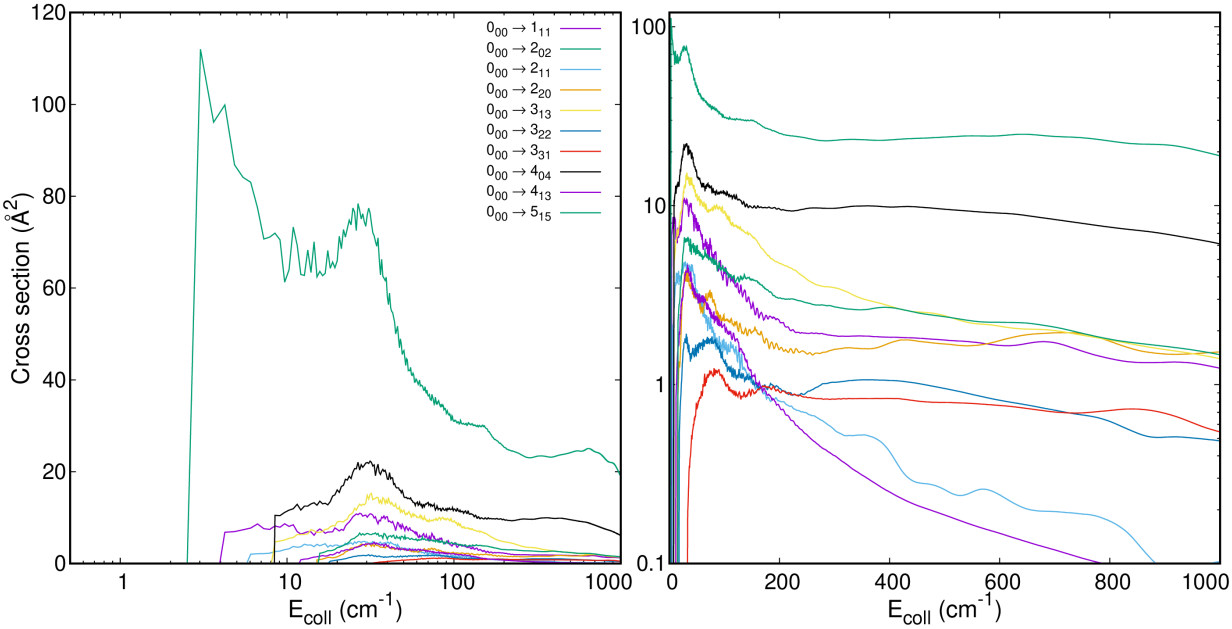

Figure 3: Inelastic cross-sections for allowed transitions from $0_{0,0}$ to low lying states for $^{16}O^{16}O^{16}O$–Ar. Panel at left uses a log-scale for the collision energy to highlight the threshold behavior. Panel at right uses a log-scale for the cross-sections to highlight the behavior of the weaker transitions.

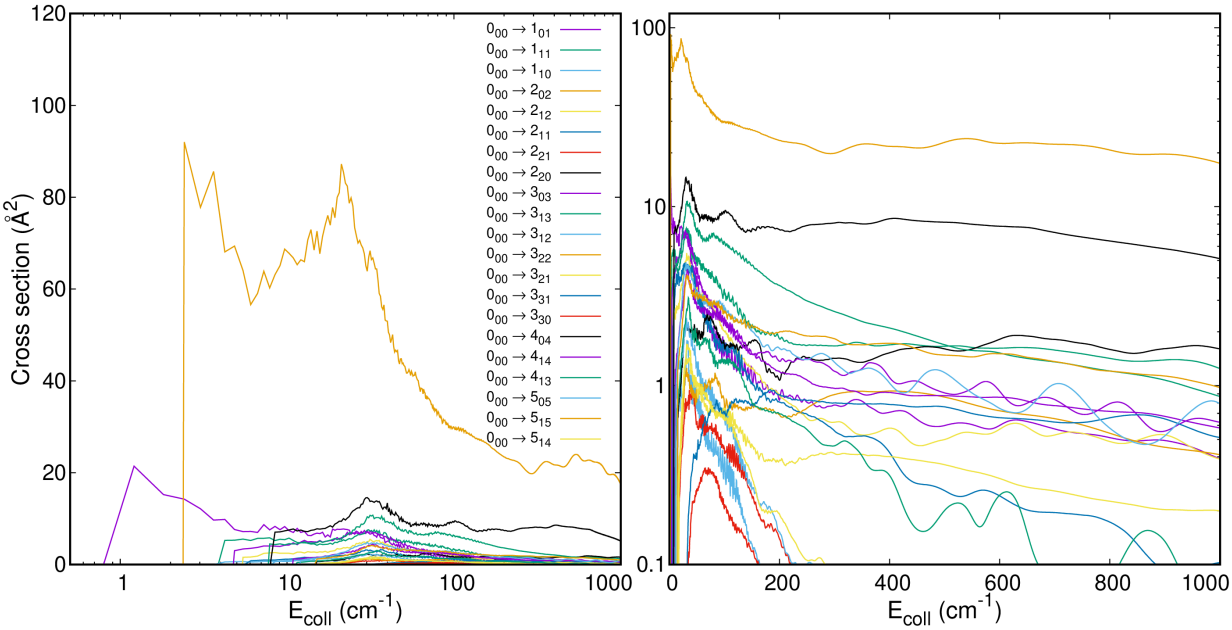

Figure 4: Inelastic cross-sections for allowed transitions from $0_{0,0}$ to low lying states for $^{16}O^{16}O^{18}O$–Ar. Panel at left uses a log-scale for the collision energy to highlight the threshold behavior. Panel at right uses a log-scale for the cross-sections to highlight the behavior of the weaker transitions.

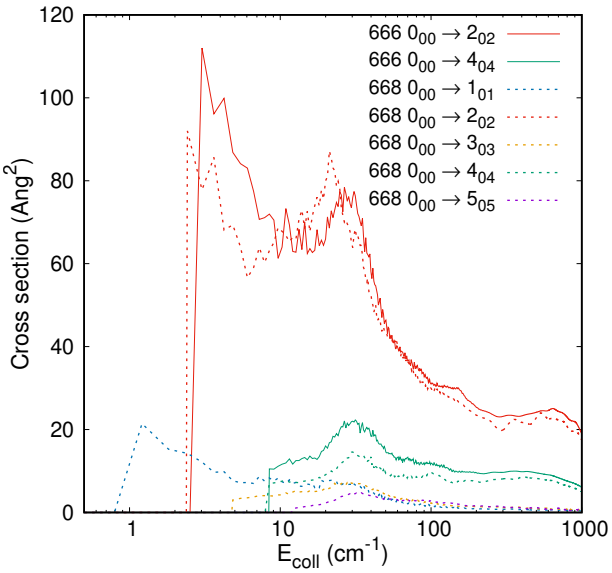

Figure 5: Comparison of transitions to j_{0,K_c} ($K_c = j$) type states for 666 (solid lines) and 668 (dashed lines). The perfect evenness of the PES for 666 is broken in 668 and the corresponding cross-sections are slightly reduced. On the other hand, in 668, states with odd values of j become allowed and make contributions not seen in 666.

The rate coefficients can be obtained by integrating the inelastic cross-sections using:

$$k_{j_{K_a,K_c}}(E) = \sqrt{8\beta^4/\pi\mu_R\beta} \int_0^\infty dE_{coll} e^{-\beta E_{coll}} E_{coll} \sigma_{j_{K_a,K_c}}(E) \ , \tag{11}$$

where β=$1/k_BT$, k_B is the Boltzmann constant. Just as Eq. 10 yields the cross section between specific initial and final states, Eq. 11 is used to evaluate each state-to-state rate. The inelastic rate coefficients for the 666 and 668 isotopologues are presented in Tables 6 and 7.

Here we discuss the temperature dependance of the rates. The propensities are most easily appreciated in the 668 results since all states are allowed. Three panels of Figure 6 plot the temperature dependance of the rates for transitions from the $0_{0,0}$ state of 668 to product states with $j = 1, 2$, and 3 respectively. As expected from the cross-sections, the rate for the $0_{0,0}$ to $2_{0,2}$ transition is by far the largest across the full temperature range of

Table 6: The inelastic collisional rate coefficients of various transitions for $^{16}O^{16}O^{16}O$–Ar as a function of temperature.

Transition	Rate coefficients (cm^3 s^{-1})							
	5K	10K	25K	50K	75K	100K	150K	200K
$0_{0,0} \rightarrow 1_{1,1}$	3.62(-12)	6.89(-12)	1.22(-11)	1.43(-11)	1.42(-11)	1.38(-11)	1.32(-11)	1.28(-11)
$0_{0,0} \rightarrow 2_{0,2}$	4.55(-11)	6.75(-11)	9.47(-11)	1.04(-10)	1.08(-10)	1.11(-10)	1.18(-10)	1.25(-10)
$0_{0,0} \rightarrow 2_{1,1}$	1.06(-12)	2.83(-12)	5.45(-12)	6.15(-12)	5.94(-12)	5.61(-12)	5.00(-12)	4.51(-12)
$0_{0,0} \rightarrow 2_{2,0}$	8.11(-14)	8.61(-13)	3.61(-12)	5.66(-12)	6.50(-12)	6.99(-12)	7.71(-12)	8.39(-12)
$0_{0,0} \rightarrow 3_{1,3}$	1.40(-12)	5.40(-12)	1.48(-11)	2.12(-11)	2.33(-11)	2.39(-11)	2.36(-11)	2.29(-11)
$0_{0,0} \rightarrow 3_{2,2}$	2.47(-14)	3.39(-13)	1.68(-12)	2.91(-12)	3.48(-12)	3.84(-12)	4.34(-12)	4.71(-12)
$0_{0,0} \rightarrow 3_{3,1}$	1.87(-16)	2.31(-14)	4.97(-13)	1.46(-12)	2.13(-12)	2.61(-12)	3.27(-12)	3.74(-12)
$0_{0,0} \rightarrow 4_{0,4}$	2.76(-12)	9.68(-12)	2.30(-11)	3.07(-11)	3.44(-11)	3.71(-11)	4.18(-11)	4.59(-11)
$0_{0,0} \rightarrow 4_{1,3}$	1.65(-13)	1.14(-12)	3.95(-12)	5.52(-12)	5.72(-12)	5.53(-12)	4.91(-12)	4.33(-12)
$0_{0,0} \rightarrow 5_{1,5}$	1.49(-13)	1.50(-12)	6.24(-12)	1.00(-11)	1.17(-11)	1.26(-11)	1.37(-11)	1.44(-11)

Table 7: The inelastic collisional rate coefficients of various transitions for $^{16}O^{16}O^{18}O$–Ar as a function of temperature.

Transition	Rate coefficients (cm^3 s^{-1})							
	5K	10K	25K	50K	75K	100K	150K	200K
$0_{0,0} \rightarrow 1_{0,1}$	6.39(-12)	7.65(-12)	8.96(-12)	8.22(-12)	7.34(-12)	6.70(-12)	5.94(-12)	5.54(-12)
$0_{0,0} \rightarrow 1_{1,1}$	2.52(-12)	4.62(-12)	8.11(-12)	9.80(-12)	1.01(-11)	1.01(-11)	1.01(-11)	1.01(-11)
$0_{0,0} \rightarrow 1_{1,0}$	3.37(-13)	7.19(-13)	1.32(-12)	1.43(-12)	1.29(-12)	1.14(-12)	8.88(-13)	7.17(-13)
$0_{0,0} \rightarrow 2_{0,2}$	4.23(-11)	6.53(-11)	9.19(-11)	9.96(-11)	1.02(-10)	1.04(-10)	1.09(-10)	1.16(-10)
$0_{0,0} \rightarrow 2_{1,2}$	9.30(-13)	2.39(-12)	5.19(-12)	6.41(-12)	6.41(-12)	6.15(-12)	5.60(-12)	5.21(-12)
$0_{0,0} \rightarrow 2_{1,1}$	4.29(-13)	1.28(-12)	3.00(-12)	3.75(-12)	3.85(-12)	3.85(-12)	3.80(-12)	3.71(-12)
$0_{0,0} \rightarrow 2_{2,1}$	1.35(-14)	1.56(-13)	7.23(-13)	1.10(-12)	1.17(-12)	1.13(-12)	1.00(-12)	8.78(-13)
$0_{0,0} \rightarrow 2_{2,0}$	4.83(-14)	4.71(-13)	2.14(-12)	3.75(-12)	4.59(-12)	5.14(-12)	6.04(-12)	6.86(-12)
$0_{0,0} \rightarrow 3_{0,3}$	1.79(-12)	4.15(-12)	7.66(-12)	8.52(-12)	8.32(-12)	8.06(-12)	7.72(-12)	7.53(-12)
$0_{0,0} \rightarrow 3_{1,3}$	1.18(-12)	3.93(-12)	1.02(-11)	1.45(-11)	1.61(-11)	1.67(-11)	1.67(-11)	1.63(-11)
$0_{0,0} \rightarrow 3_{1,2}$	2.29(-13)	8.44(-13)	2.00(-12)	2.34(-12)	2.20(-12)	1.99(-12)	1.63(-12)	1.36(-12)
$0_{0,0} \rightarrow 3_{2,2}$	1.43(-14)	1.96(-13)	9.92(-13)	1.77(-12)	2.21(-12)	2.54(-12)	3.09(-12)	3.53(-12)
$0_{0,0} \rightarrow 3_{2,1}$	1.52(-14)	2.25(-13)	1.07(-12)	1.64(-12)	1.82(-12)	1.91(-12)	2.01(-12)	2.08(-12)
$0_{0,0} \rightarrow 3_{3,1}$	1.36(-16)	1.51(-14)	3.13(-13)	1.01(-13)	1.61(-12)	2.08(-12)	2.78(-12)	3.27(-12)
$0_{0,0} \rightarrow 3_{3,0}$	7.21(-17)	8.49(-15)	1.57(-13)	3.74(-13)	4.53(-13)	4.74(-13)	4.69(-13)	4.53(-13)
$0_{0,0} \rightarrow 4_{0,4}$	1.70(-12)	5.85(-12)	1.43(-11)	2.03(-11)	2.37(-11)	2.65(-11)	3.13(-11)	3.54(-11)
$0_{0,0} \rightarrow 4_{1,4}$	2.18(-13)	1.19(-12)	3.77(-12)	5.42(-12)	5.93(-12)	6.09(-12)	6.15(-12)	6.14(-12)
$0_{0,0} \rightarrow 4_{1,3}$	9.57(-14)	6.40(-13)	2.28(-12)	3.33(-12)	3.60(-12)	3.62(-12)	3.45(-12)	3.21(-12)
$0_{0,0} \rightarrow 5_{0,5}$	1.69(-13)	1.18(-12)	4.19(-12)	6.23(-12)	6.97(-12)	7.28(-12)	7.49(-12)	7.51(-12)
$0_{0,0} \rightarrow 5_{1,5}$	8.46(-14)	8.15(-13)	3.50(-12)	5.72(-12)	6.76(-12)	7.40(-12)	8.24(-12)	8.79(-12)
$0_{0,0} \rightarrow 5_{1,4}$	2.24(-14)	2.70(-13)	1.19(-12)	1.70(-12)	1.73(-12)	1.65(-12)	1.42(-12)	1.23(-12)

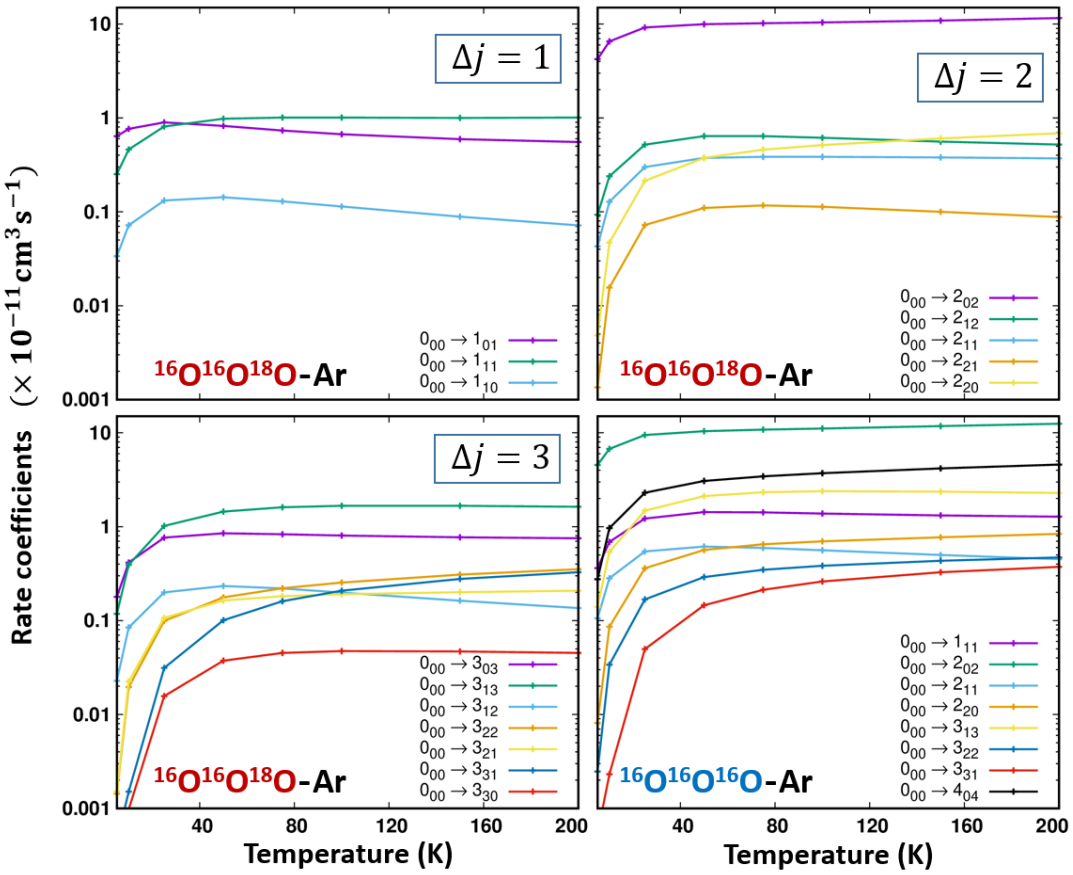

Figure 6: Three panels show the detailed rates for $\Delta j = 1$–3 transitions in the 668 isotopologue. A fourth panel (bottom-right) combines the results for the sparser set of low-lying states in 666.

5 K to 200 K. Of course for even lower temperatures, because of the lower threshold to $1_{0,1}$ (as seen in Figure 4), one should expect the rate for the $0_{0,0}$ to $1_{0,1}$ transition to be largest. Indeed, we have confirmed that this is the case up to 2 K, above which it is surpassed by $2_{0,2}$, as seen in Table 7. At 5 K the rate to $2_{0,2}$ is already more than five times larger. This is partly due to the strong suppression of $1_{0,1}$ due to the near symmetry of the PES. For the *odd* Δj transitions, lacking the one dominant process seen in the *even* Δj transitions, at the lowest temperatures the rates for transitions to j_{0,K_c} ($K_c = j$) states are largest, but are overtaken at high temperature by rates to states with j_{1,K_c} ($K_c = j$). For 666 (also shown in Figure 6), the results are quite similar although half the states are missing and the rate

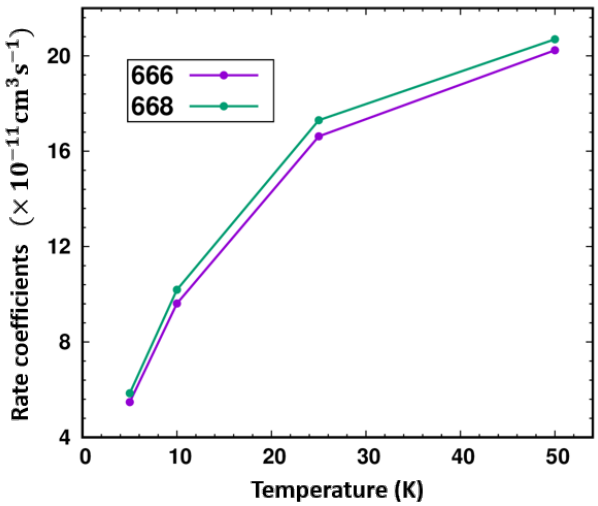

Figure 7: The total rate of state-changing collisions from the $0_{0,0}$ ground initial state is compared for the 666 and 668 isotopologues as a function of temperature. The 668 isotopologue is seen to undergo inelastic collisions at a slightly higher total rate (see text).

of state-changing collisions is dominated by transitions to the j_{0,K_c} $(K_c = j)$ states.

Given the state-to-state rates for the 666 and 668 isotopologues, it is of interest to determine whether or not the total rate of state-changing collisions is generally larger for 668, possibly playing a role in enhancing the stabilization of 668 during ozone formation, and thus contributing to the observed ozone isotopic anomaly discussed in the Introduction. Of course the relevant process of collisional stabilization in the stratosphere involves highly excited resonance states of (O_3^*), but the effects of symmetry breaking and increased state density are still applicable. In Figure 7, by combining all of the rates for each system (from the initial state to all product channels), the total rate of state changing collisions is compared for 666 and 668. It is important to note the behavior of the temperature dependance of individual state-to-state rates shown in the previous figures. Generally, at a temperature corresponding to collision energies exceeding the energy threshold for a given transition, there is a rapid initial rise in the rate, which typically then levels off and perhaps drops at higher temperatures. Since results were only obtained here for a complete set of product states up to 20.0 cm^{-1}, the relative total rates can only be rigorously assessed at the lowest temperatures, since at higher temperatures missing product channels become

important. Indeed, for temperatures up to 25 K, for which a complete set of product channels is included, the total rate of state changing collisions is about 5–7 % larger for 668 than for 666. This is significant and on the order of the isotopic enhancements observed in the stratosphere. As has been pointed out previously, since ozone is continuously destroyed and then regenerated, even a small bias can lead to accumulation of the favored isotopologues.

Conclusion

A possible key to understanding the ozone isotopic anomaly in the atmosphere, is understanding the relative efficiencies of the stabilization step for different isotopologues in the formation process of ozone. Stabilization involves the collisional cooling of a rovibrational resonance state from above the dissociation threshold, into the manifold of bound states. Current models approximate the cooling efficiencies for different isotopologues as equal. Direct simulation of these quantum scattering processes would be exceedingly demanding computationally and require a fully flexible 6D PES, which is not yet available.

Asymmetric heavy isotopologues such as $^{16}O^{16}O^{18}O$ (668) have more than twice the density of states as the parent $^{16}O^{16}O^{16}O$ (666) isotopologue mainly due a doubling of the number of states allowed by nuclear spin statistics for bosons, and to a small extent, the mass-related changes in rotational constants. The increased state density is found throughout all of the bound states and not just those near dissociation. Benchmark studies in atom-diatom systems have found significantly different scattering dynamics upon isotopic substitution for precisely these reasons. Qualitative aspects of the symmetry-breaking and changes in allowed-state densities are similar for 667 and 668, and thus assigning some importance to collisional cooling efficiency is consistent with the largely mass-independent nature of this phenomenon for various isotopologues.

In this study, we have compared the state-to-state scattering cross-sections and rates between low-lying states for rotationally inelastic collisions between two isotopologues of

ozone (symmetric 666 and asymmetric 668) and an argon atom. The fully quantum time-dependent MCTDH approach was employed for the scattering calculations, using our new highly accurate 3D (rigid rotor) PES. It was found that the strong propensities for $\Delta j = 2$ transitions in 666, governed by the evenness of the PES, are relaxed somewhat in collisions with the 668 isotopologue as the symmetry of the PES is slightly broken and newly allowed states become available as product channels. Comparing the total rate of state-changing collisions for 668 with 666, it was found that the total rate for 668 is indeed about 5–7 % larger. Some of this difference might be attributable to the small change in the reduced mass of the collision system for heavier isotopologues. Since ozone is destroyed and then regenerated many times through the Chapman cycle, even a small bias can lead to accumulation of the favored isotopologues. It is of interest in future work to include the differing collisional efficiencies in kinetic models. It is also desirable to extend the collisional studies into the more relevant high-lying states. The stratospherically relevant dynamics of interest here are de-excitation, the rates of which are connected (to excitation rates) through the principle of detailed balance. The cost of performing rigorous quantum scattering calculations for O_3–Ar is still quite high. Another avenue of research currently underway is to study the dynamics of collisions for O_2–Ar, comparing $^{16}O^{16}O$–Ar with $^{16}O^{18}O$–Ar and $^{18}O^{18}O$–Ar. Those calculations are much more affordable despite the slight added complexity of the fine-structure introduced by the triplet spin-state. Many of the same factors are relevant since asymmetric isotopic substitution in O_2 also shifts the center-of-mass, breaking the evenness of the PES, and roughly doubles the density of states. There it will be affordable to analyze both excitation and de-excitation processes from a wide variety of initial states. It will be particularly important to understand the differences in dynamics between the linear rotor (O_2) and asymmetric top (O_3), since despite some similarities, no anomalous fractionation has been observed in O_2.

Acknowledgements

This work was supported by the US National Science Foundation (No. CHE-1566246).

References

(1) Thiemens, M. H. Mass-independent isotope effects in planetary atmospheres and the early solar system. *Science* **1999**, *283*, 341–345.

(2) Mauersberger, K.; Erbacher, B.; Krankowsky, D.; Günther, J.; Nickel, R. Ozone isotope enrichment: Isotopomer-specific rate coefficients. *Science* **1999**, *283*, 370–372.

(3) Sun, Z.; Yu, D.; Xie, W.; Hou, J.; Dawes, R.; Guo, H. Kinetic isotope effect of the $^{16}O+^{36}O_2$ and $^{18}O+^{32}O_2$ isotope exchange reactions: Dominant role of reactive resonances revealed by an accurate time-dependent quantum wavepacket study. *J. Chem. Phys.* **2015**, *142*, 174312.

(4) Lahankar, S. A.; Zhang, J.; Minton, T. K.; Guo, H.; Lendvay, G. Dynamics of the O-Atom Exchange Reaction $^{16}O(^3P) + {}^{18}O^{18}O(^3\Sigma_g^-) \rightarrow {}^{16}O^{18}O(^3\Sigma_g^-) + {}^{18}O(^3P)$ at Hyperthermal Energies. *J. Phys. Chem. A* **2016**, *120*, 5348–5359.

(5) Chakraborty, S.; Bhattacharya, S. Oxygen isotopic fractionation during UV and visible light photodissociation of ozone. *J. Chem. Phys.* **2003**, *118*, 2164–2172.

(6) Chakraborty, S.; Bhattacharya, S. Oxygen isotopic anomaly in surface induced ozone dissociation. *Chem. Phys. Lett.* **2003**, *369*, 662–667.

(7) Bhattacharya, S.; Chakraborty, S.; Savarino, J.; Thiemens, M. H. Low-pressure dependency of the isotopic enrichment in ozone: Stratospheric implications. *Geophys. Res.: Atmos.* **2002**, *107*, 4675.

(8) Babikov, D.; Kendrick, B. K.; Walker, R. B.; T Pack, R.; Fleurat-Lesard, P.; Schinke, R. Metastable states of ozone calculated on an accurate potential energy surface. *J. Chem. Phys.* **2003**, *118*, 6298–6308.

(9) Babikov, D.; Kendrick, B.; Walker, R.; Schinke, R.; Pack, R. Quantum origin of an anomalous isotope effect in ozone formation. *Chem. Phys. Lett.* **2003**, *372*, 686–691.

(10) Babikov, D.; Kendrick, B. K.; Walker, R. B.; T Pack, R.; Fleurat-Lesard, P.; Schinke, R. Formation of ozone: Metastable states and anomalous isotope effect. *J. Chem. Phys.* **2003**, *119*, 2577–2589.

(11) Teplukhin, A.; Babikov, D. Several levels of theory for description of isotope effects in ozone: Symmetry effect and Mass effect. *J. Phys. Chem. A* **2018**, *122*, 9177–9190.

(12) Gao, Y. Q.; Marcus, R. Strange and unconventional isotope effects in ozone formation. *Science* **2001**, *293*, 259–263.

(13) Gao, Y.; Marcus, R. On the theory of the strange and unconventional isotopic effects in ozone formation. *J. Chem. Phys.* **2002**, *116*, 137–154.

(14) Gao, Y. Q.; Chen, W.-C.; Marcus, R. A theoretical study of ozone isotopic effects using a modified ab initio potential energy surface. *J. Chem. Phys.* **2002**, *117*, 1536–1543.

(15) Hathorn, B.; Marcus, R. An intramolecular theory of the mass-independent isotope effect for ozone. II. Numerical implementation at low pressures using a loose transition state. *J. Chem. Phys.* **2000**, *113*, 9497–9509.

(16) Mauersberger, K. Measurement of heavy ozone in the stratosphere. *Geophys. Res. Lett.* **1981**, *8*, 935–937.

(17) Mauersberger, K. Ozone isotope measurements in the stratosphere. *Geophys. Res. Lett.* **1987**, *14*, 80–83.

(18) Thiemens, M. H.; Heidenreich, J. E. The mass-independent fractionation of oxygen: A novel isotope effect and its possible cosmochemical implications. *Science* **1983**, *219*, 1073–1075.

(19) Morton, J.; Barnes, J.; Schueler, B.; Mauersberger, K. Laboratory studies of heavy ozone. *J. Geophys. Res.:Atmos.* **1990**, *95*, 901–907.

(20) Anderson, S.; Hülsebusch, D.; Mauersberger, K. Surprising rate coefficients for four isotopic variants of O+O_2+M. *J. Chem. Phys.* **1997**, *107*, 5385–5392.

(21) Janssen, C.; Guenther, J.; Krankowsky, D.; Mauersberger, K. Relative formation rates of $^{50}O_3$ and $^{52}O_3$ in ^{16}O–^{18}O mixtures. *J. Chem. Phys.* **1999**, *111*, 7179–7182.

(22) Janssen, C.; Guenther, J.; Krankowsky, D.; Mauersberger, K. Erratum: "Relative formation rates of $^{50}O_3$ and $^{52}O_3$ in ^{16}O–^{18}O mixtures" [J. Chem. Phys. 111, 7179 (1999)]. *J. Chem. Phys.* **2000**, *112*, 11109–11109.

(23) Wolf, S.; Bitter, M.; Krankowsky, D.; Mauersberger, K. Multi-isotope study of fractionation effects in the ozone formation process. *J. Chem. Phys.* **2000**, *113*, 2684–2686.

(24) Chapman, S. A theory of upperatmospheric ozone. *Mem. Roy. Meteor.* **1930**, *3*, 103–125.

(25) Heidenreich III, J. E.; Thiemens, M. H. A non-mass-dependent oxygen isotope effect in the production of ozone from molecular oxygen: The role of molecular symmetry in isotope chemistry. *J. Chem. Phys.* **1986**, *84*, 2129–2136.

(26) Guenther, J.; Krankowsky, D.; Mauersberger, K. Third-body dependence of rate coefficients for ozone formation in ^{16}O–^{18}O mixtures. *Chem. Phys. Lett.* **2000**, *324*, 31–36.

(27) Dawes, R.; Lolur, P.; Ma, J.; Guo, H. Communication: Highly accurate ozone formation potential and implications for kinetics. *J. Chem. Phys.* **2011**, *135*, 081102.

(28) Dawes, R.; Lolur, P.; Li, A.; Jiang, B.; Guo, H. Communication: An accurate global potential energy surface for the ground electronic state of ozone. *J. Chem. Phys.* **2013**, *139*, 201103.

(29) Powell, A. D.; Dattani, N. S.; Spada, R. F.; Machado, F. B.; Lischka, H.; Dawes, R. Investigation of the ozone formation reaction pathway: Comparisons of full configuration interaction quantum Monte Carlo and fixed-node diffusion Monte Carlo with contracted and uncontracted MRCI. *J. Chem. Phys.* **2017**, *147*, 094306.

(30) Tyuterev, V. G.; Kochanov, R. V.; Tashkun, S. A.; Holka, F.; Szalay, P. G. New analytical model for the ozone electronic ground state potential surface and accurate ab initio vibrational predictions at high energy range. *J. Chem. Phys.* **2013**, *139*, 134307.

(31) Li, Y.; Sun, Z.; Jiang, B.; Xie, D.; Dawes, R.; Guo, H. Communication: Rigorous quantum dynamics of O+O_2 exchange reactions on an ab initio potential energy surface substantiate the negative temperature dependence of rate coefficients. *J. Chem. Phys.* **2014**, *141*, 081102.

(32) Xie, W.; Liu, L.; Sun, Z.; Guo, H.; Dawes, R. State-to-state reaction dynamics of ^{18}O+ $^{32}O_2$ studied by a time-dependent quantum wavepacket method. *J. Chem. Phys.* **2015**, *142*, 064308.

(33) Honvault, P.; Guillon, G.; Kochanov, R.; Tyuterev, V. Quantum mechanical study of the ^{16}O+ ^{18}O^{18}O$\rightarrow$ ^{16}O^{18}O+ ^{18}O exchange reaction: Integral cross sections and rate constants. *J. Chem. Phys.* **2018**, *149*, 214304.

(34) Ivanov, M. V.; Babikov, D. Efficient quantum-classical method for computing thermal rate constant of recombination: Application to ozone formation. *J. Chem. Phys.* **2012**, *136*, 184304.

(35) Ivanov, M. V.; Babikov, D. On molecular origin of mass-independent fractionation of

oxygen isotopes in the ozone forming recombination reaction. *Proc. Natl. Acad. Sci.* **2013**, *110*, 17708–17713.

(36) Ivanov, M.; Schinke, R. Vibrational energy transfer in Ar–O_3 collisions: comparison of rotational sudden, breathing sphere, and classical calculations. *Mol. Phys.* **2010**, *108*, 259–268.

(37) Xie, T.; Bowman, J. M. Quantum inelastic scattering study of isotope effects in ozone stabilization dynamics. *Chem. Phys. Lett.* **2005**, *412*, 131–134.

(38) Schinke, R.; Grebenshchikov, S. Y.; Ivanov, M.; Fleurat-Lessard, P. Dynamical studies of the ozone isotope effect: A status report. *Ann. Rev. Phys. Chem.* **2006**, *57*, 625–661.

(39) Dumouchel, F.; Kłos, J.; Toboła, R.; Bacmann, A.; Maret, S.; Hily-Blant, P.; Faure, A.; Lique, F. Fine and hyperfine excitation of NH and ND by He: On the importance of calculating rate coefficients of isotopologues. *J. Chem. Phys.* **2012**, *137*, 114306.

(40) Flower, D.; Lique, F. Excitation of the hyperfine levels of ^{13}CN and C^{15}N in collisions with H_2 at low temperatures. *Mon. Not. R. Astron. Soc.* **2014**, *446*, 1750–1755.

(41) Dumouchel, F.; Lique, F.; Spielfiedel, A.; Feautrier, N. Hyperfine excitation of C_2H and C_2D by para-H_2. *Mon. Not. R. Astron. Soc.* **2017**, *471*, 1849–1855.

(42) Quack, M. Detailed symmetry selection rules for reactive collisions. *Mol. Phys.* **1977**, *34*, 477–504.

(43) Sur, S.; Quintas-Sánchez, E.; Ndengué, S. A.; Dawes, R. Development of a potential energy surface for the O_3–Ar system: rovibrational states of the complex. *Phys. Chem. Chem. Phys.* **2019**, *21*, 9168.

(44) DeLeon, R. L.; Mack, K. M.; Muenter, J. Structure and properties of the argon–ozone van der Waals molecule. *J. Chem. Phys.* **1979**, *71*, 4487–4491.

(45) Gatti, F.; Otto, F.; Sukiasyan, S.; Meyer, H.-D. Rotational excitation cross sections of para-H_2+ para-H_2 collisions. A full-dimensional wave-packet propagation study using an exact form of the kinetic energy. *J. Chem. Phys.* **2005**, *123*, 174311.

(46) Otto, F.; Gatti, F.; Meyer, H.-D. Rotational excitations in para-H_2+ para-H_2 collisions: Full-and reduced-dimensional quantum wave packet studies comparing different potential energy surfaces. *J. Chem. Phys.* **2008**, *128*, 064305.

(47) Otto, F.; Gatti, F.; Meyer, H.-D. Erratum:"Rotational excitations in para-H_2+ para-H_2 collisions: Full-and reduced-dimensional quantum wave packet studies comparing different potential energy surfaces"[J. Chem. Phys. 128, 064305 (2008)]. *J. Chem. Phys.* **2009**, *131*, 049901.

(48) Ndengué, S.; Scribano, Y.; Gatti, F.; Dawes, R. State-to-state inelastic rotational cross sections in five-atom systems with the multiconfiguration time dependent Hartree method. *J. Chem. Phys.* **2019**, *151*, 134301.

(49) Jasper, A. W.; Pelzer, K. M.; Miller, J. A.; Kamarchik, E.; Harding, L. B.; Klippenstein, S. J. Predictive a priori pressure-dependent kinetics. *Science* **2014**, *346*, 1212–1215.

(50) Alexander, M. H.; Jendrek, E. F.; Dagdigian, P. J. Validity of energy gap representations of rotationally inelastic cross sections between polar molecules. *J. Chem. Phys.* **1980**, *73*, 3797–3803.

(51) Alexander, M. H.; Hall, G. E.; Dagdigian, P. J. The approach to equilibrium: Detailed balance and the master equation. *J. Chem. Educ.* **2011**, *88*, 1538–1543.

(52) Quintas-Sánchez, E.; Dawes, R. AUTOSURF: A Freely Available Program To Construct Potential Energy Surfaces. *J. Chem. Inf. Model.* **2019**, *59*, 262–271.

(53) Meyer, H.-D.; Gatti, F.; Worth, G. A. *Multidimensional quantum dynamics*; John Wiley & Sons, 2009.

(54) Beck, M. H.; Jäckle, A.; Worth, G.; Meyer, H.-D. The multiconfiguration time-dependent Hartree (MCTDH) method: a highly efficient algorithm for propagating wavepackets. *Phys. Rep.* **2000**, *324*, 1–105.

(55) Gatti, F.; Meyer, H.-D. Intramolecular vibrational energy redistribution in toluene: a nine-dimensional quantum mechanical study using the MCTDH algorithm. *Chem. Phys.* **2004**, *304*, 3–15.

(56) Sadri, K.; Lauvergnat, D.; Gatti, F.; Meyer, H.-D. Rovibrational spectroscopy using a kinetic energy operator in Eckart frame and the multi-configuration time-dependent Hartree (MCTDH) approach. *J. Chem. Phys.* **2014**, *141*, 114101.

(57) Worth, G.; Beck, M.; Jäckle, A.; Meyer, H.-D. The MCTDH Package, Version 8.2, (2000), University of Heidelberg, Heidelberg, Germany. H.-D. Meyer, Version 8.3 (2002), Version 8.4 (2007), O. Vendrell and H.-D. Meyer, Version 8.5 (2011). 2007; See http://mctdh.uni-hd.de.

(58) Malenda, R.; Gatti, F.; Meyer, H.-D.; Talbi, D.; Hickman, A. Comparison of the multi-configuration, time-dependent Hartree (MCTDH) method with the Arthurs and Dalgarno coupled-channel method for rotationally inelastic scattering. *Chem. Phys. Lett.* **2013**, *585*, 184–188.

(59) Ndengue, S. A.; Dawes, R.; Gatti, F. Rotational Excitations in CO–CO Collisions at Low Temperature: Time-Independent and Multiconfigurational Time-Dependent Hartree Calculations. *J. Phys. Chem. A* **2015**, *119*, 7712–7723.

(60) Ndengué, S.; Dawes, R.; Gatti, F.; Meyer, H.-D. Atom-triatom rigid rotor inelastic scattering with the MultiConfiguration Time Dependent Hartree approach. *Chem. Phys. Lett.* **2017**, *668*, 42–46.

(61) Gatti, F.; Iung, C. Exact and constrained kinetic energy operators for polyatomic molecules: The polyspherical approach. *Phys. Rep.* **2009**, *484*, 1–69.

(62) Depannemaecker, J.-C.; Bellet, J. Rotational spectra of $^{16}O_3$ and of the five ^{18}O isotopic species. *J. Mol. Spec.* **1977**, *66*, 106–120.

(63) Jäckle, A.; Meyer, H.-D. Product representation of potential energy surfaces. *J. Chem. Phys.* **1996**, *104*, 7974–7984.

(64) Jäckle, A.; Meyer, H.-D. Product representation of potential energy surfaces. II. *J. Chem. Phys.* **1998**, *109*, 3772–3779.

(65) Leforestier, C. Grid method for the Wigner functions. Application to the van der Waals system Ar–H_2O. *J. Chem. Phys.* **1994**, *101*, 7357–7363.

(66) Füchsel, G.; Thomas, P. S.; den Uyl, J.; Öztürk, Y.; Nattino, F.; Meyer, H.-D.; Kroes, G.-J. Rotational effects on the dissociation dynamics of CHD_3 on Pt(111). *Phys. Chem. Chem. Phys.* **2016**, *18*, 8174–8185.

(67) Flaud, J.; Bacis, R. The ozone molecule: infrared and microwave spectroscopy. *Spec. Acta Part A: Mol. Spec.* **1998**, *54*, 3–16.

(68) Meyer, H.-D.; Worth, G. A. Quantum molecular dynamics: propagating wavepackets and density operators using the multiconfiguration time-dependent Hartree method. *Theor. Chem. Acc.* **2003**, *109*, 251–267.

(69) Meyer, H.-D.; Le Quéré, F.; Léonard, C.; Gatti, F. Calculation and selective population of vibrational levels with the Multiconfiguration Time-Dependent Hartree (MCTDH) algorithm. *Chem. Phys.* **2006**, *329*, 179–192.

(70) Ndengué, S.; Dawes, R.; Wang, X.-G.; Carrington Jr, T.; Sun, Z.; Guo, H. Calculated vibrational states of ozone up to dissociation. *J. Chem. Phys.* **2016**, *144*, 074302.

(71) Borowski, P.; Andersson, K.; Malmqvist, P.-Å.; Roos, B. Vibrational frequencies of ozone: A multiconfigurational approach. *J. Chem. Phys.* **1992**, *97*, 5568–5577.

(72) Tannor, D. J.; Weeks, D. E. Wave packet correlation function formulation of scattering theory: The quantum analog of classical S-matrix theory. *J. Chem. Phys.* **1993**, *98*, 3884–3893.